

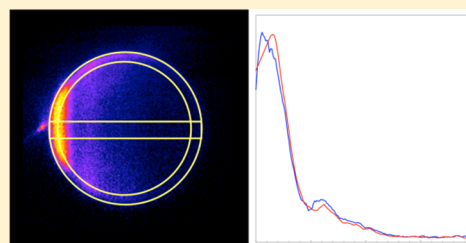
Direct Extraction of Alignment Moments from Inelastic Scattering Images

Arthur G. Suits,^{*,†,‡} Chandan Kumar Bishwakarma,[†] Lei Song,[†] Gerrit C. Groenenboom,[†] Ad van der Avoird,[†] and David H. Parker^{*,†}

[†]Institute for Molecules and Materials, Radboud University, 6525, Nijmegen, The Netherlands

[‡]Department of Chemistry, Wayne State University, Detroit, Michigan 48202, United States

ABSTRACT: We present a novel means of analyzing velocity-map images of angular momentum polarization in inelastic scattering. In this approach, linear combinations of angular distributions obtained by integrating select regions of images for two probe laser polarizations directly yield the alignment-free differential cross sections and the differential alignment moments. No fitting is needed in the analysis. The method relies on the fact that the angular distribution for out-of-plane scattering is encoded in the distribution along the relative velocity vector, and this may be recovered quantitatively owing to the redundancy of the in-plane and out-of-plane scattering for the horizontal polarization case.



INTRODUCTION

Despite two decades of active investigation, imaging studies of inelastic scattering continue to offer surprising new insights into fundamental aspects of atomic and molecular interactions.^{1–7} These studies allow stringent tests of the quality of electronic structure calculations and stimulate efforts to combine the intuition afforded by classical treatments with the rigors of a full quantum description. Among the more intriguing such examples in recent years has been the direct detection of collision-induced polarization in scattering.^{8–15} The power of imaging in these experiments is that it combines a spectroscopic probe (i.e., resonance-enhanced ionization) with angular distribution measurements, yielding a molecular-frame description of the scattering event.^{16,17} The study of collision-induced angular momentum polarization is an example of three-vector correlation (the initial relative velocity vector, the final relative velocity vector, and the angular momentum projection), and their correlations are simultaneously measured.^{11,18–22} Meyer reported early investigations of rotational alignment in state-resolved scattering of NH₃ and NO,^{8,23} which was followed by imaging studies by Chandler, Cline, and co-workers on the argon–NO system.^{9,13} Studies by Chandler and Cline and co-workers also showed that such collisions could give rise locally to rotational orientation, and the sense of this orientation and its angular distribution could be measured using circularly polarized probe lasers. This continues to be an active area of investigation.^{7,12} Very recently, Chandler and co-workers have studied scattering of electronically excited NO, even examining alignment in that system,^{6,24} and Brouard and co-workers have revisited the issue of rotational alignment in the argon–NO system and combined this both with full quantum calculations and with a quasi-quantum treatment.^{10,14,25}

In essentially all of these inelastic scattering alignment studies, the analysis is performed by taking difference images

obtained with probe polarization parallel to the detector (“H”) or perpendicular to the detector (“V”). These difference images are then fitted using various means to extract the alignment moments. For rotational alignment with one-photon probe there are two such moments, $A_0^{(2)}$ and $A_{2+}^{(2)}$ (we will employ the Hertel–Stoll renormalized polarization-dependent differential cross sections^{26,27}) whose angular distributions are reported and related to classical treatments or to full time-independent quantum scattering calculations. Although these approaches to the analysis are clearly successful, we are naturally led to wonder if there might be a more direct way to extract these distributions from high quality scattering data rather than through fitting methods. With the remarkable resolution of velocity-map imaging and the simple clarity of these images such an objective seems attainable. If we are successful, any structures in the distributions will appear automatically and we need not wonder if our analysis has overlooked some or artificially imposed others. In this paper we show just such a direct means of extracting the three key distributions, the differential cross sections (DCS) and the $A_0^{(2)}$ and $A_{2+}^{(2)}$ moments, simply through linear combinations of angular distributions obtained by integrating various regions of images obtained for H and V polarization. We will illustrate this using a pair of images for final $j_{\text{CO}} = 9$, obtained for scattering of CO with argon at a collision energy of 700 cm^{−1}, and we compare our extracted distributions with quantum scattering calculations for this single rotational level. This level is chosen as it has broad scattering and is spectroscopically well-isolated. A full

Special Issue: Jean-Michel Mestdagh Festschrift

Received: September 16, 2014

Revised: November 4, 2014

Published: November 7, 2014

presentation of all the scattering results for the system and a detailed comparison to theory will be reported in a future publication.

■ EXPERIMENTAL METHODS

The data were collected in a rotatable crossed molecular beam machine using $1 + 1'$ VUV REMPI ionization of the scattered products with velocity-map imaging detection. We use two skimmed supersonic beams, one of neat argon produced from a Nijmegen pulsed valve²⁸ and the other of 5% CO seeded in argon produced from a Jordan pulsed valve. The backing pressure for the expansion was 1 bar for both colliding partners. The pulse duration of the Nijmegen pulsed valve is about 50 μ s and the pulse duration of the Jordan valve is about 60 μ s. The source chamber that houses the primary beam (CO) was differentially pumped and the molecular beam passed through a skimmer of aperture diameter 2.5 mm positioned 7 cm away from the nozzle. The secondary molecular beam (Ar) source was mounted in the differentially pumped rotatable chamber positioned 3 cm from the skimmer of aperture diameter 2.5 mm. Turbo molecular pumps pumped all the three chambers. The two molecular beams and the VUV laser were coplanar parallel to the detector and were optimally aligned to ensure the best signal. We have used four-wave difference mixing in xenon to produce tunable VUV light.^{29,30} We used two dye lasers: one (Scanmate) was fixed near the xenon resonance at 249.618 nm (ω_1) and the other dye laser (Fine Adjustment) tuned around 650 nm (ω_2) to produce tunable VUV (ω_{VUV}) light around 155 nm. The 355 and 532 nm output from an Nd:YAG laser (Continuum Powerlite 9010) were used to pump the two dye lasers. The two beams were combined at a 248 dichroic mirror transparent to visible light and both beams subsequently focused into the Xe gas (30 mbar) contained in a stainless steel cell with a $f = 100$ mm plano-convex lens. A lens of focal length $f = 1500$ mm is placed 1000 mm away from the stainless steel cell to collimate only the visible light so that 249 and 650 nm will focus at the same point inside the cell. To study alignment effects, we have used horizontal and vertical polarization of the VUV laser. The VUV was focused onto the interaction region by a magnesium fluoride lens. Its orientation was adjusted so that it did not alter the polarization of the visible and UV beams, and photodissociation images of OCS were used to confirm the desired polarization of VUV laser.³¹ Separate images were recorded independently for H and V polarization using a wave plate to rotate the polarization of the visible beam, which directly determines the VUV beam polarization. We chose the Q branch for our data collection, as it is well resolved and it shows greater sensitivity to alignment effects compared to P and R branch transitions. The laser and both molecular beams were operated at 10 Hz. The scattered product was ionized and was extracted by a velocity-map imaging ion lens.¹⁷ After 85 cm free flight along the time-of-flight tube, the 3-D ion sphere was projected onto a 2-D detector, which is read by a CCD camera. Application of gating enables us to select our required mass and filter out the background ions of other masses. Scattered CO molecules were probed by the VUV laser on the $A^1\Pi-X^1\Sigma^+$ (0–0) transitions.

■ THEORETICAL METHODS

Integral and differential state-to-state cross sections for CO–Ar collisions and the alignment of CO after the collision were computed with the close-coupling method. The intermolecular

potential used in the calculations was obtained by Pedersen et al. from *ab initio* electronic structure calculations with the coupled cluster method.³² We refer to this reference for details of these calculations and the analytic fit of the potential. Their three-dimensional (3D) CO–Ar potential depends on the two intermolecular Jacobi coordinates, as well as on the CO bond length r . We used the 2D potential also given in ref 32 that was obtained by averaging the 3D potential over the ground vibrational ($v = 0$) state of CO.

The close-coupling equations were solved with the renormalized Numerov propagator, with R ranging from 4 to 40 a_0 in 900 equal-sized steps. All rotational states of CO up to $j = 25$ were included and all partial wave contributions up to a total angular momentum of $J = 200$ were taken into account.

The experimental collision energy was estimated to be 700 cm^{-1} , but there is a certain spread in this energy. Hence, the calculations were performed for three different collision energies, 650, 700, and 750 cm^{-1} , and the cross sections were averaged with weights of 25, 50, and 25%, respectively.

The state-to-state cross sections and CO alignment moments (discussed below) were computed for initial CO states with $j = 0$ and $j = 1$ and for all final j states open at the given collision energies. Our measurements showed that the incoming CO beam contained 80% of $j = 0$ and 20% of $j = 1$, and so we averaged the calculated results over the initial $j = 0$ and $j = 1$ states of CO with these percentages. The results discussed below refer in particular to a final CO state with $j = 9$.

The alignment moments $A_0^{(2)}$ and $A_{2+}^{(2)}$ are the irreducible components of the scattering density matrix.¹⁰ The diagonal elements of this density matrix appear in the moment $A_0^{(2)}$ and represent the populations in the different magnetic quantum levels, whereas the off-diagonal elements appearing in the $A_{2+}^{(2)}$ moment reveal information about the coherences existing between different eigenstates, which are essential for the azimuthal polarization.²⁷ The scattering angle dependent density matrix is expressed in the scattering amplitudes related to the S-matrix, after undoing the angular momentum coupling used in the close-coupling calculations for different total angular momenta J .^{15,33} This uncoupling transformation is needed to resolve the different magnetic (m_j) sublevels of the final j states, as well as the scattering angle dependence of the DCSs and alignment moments.

■ RESULTS AND DISCUSSION

Overview. Our objective is to extract the DCS and the rank 2 alignment moments directly from inelastic scattering data. Our approach is to use Q-branch images for perpendicular probe transitions and consider horizontal (H) and vertical (V) polarization, where H refers to the probe polarization lying parallel to the plane of the image, and V, normal to that plane. The images that we will use for demonstration are given in Figure 1. These were obtained via the Q(9) transition of CO via the A state as described in the Experimental Methods. The difference in the appearance of these two images is a direct manifestation of angular momentum polarization. In its absence, these images would be identical. The asymmetry across the relative velocity vector arises owing to the fact that we detect product density, so the products that are slower in the laboratory frame are detected more efficiently. This is the familiar density-to-flux issue that is always faced in such studies. We find it can readily be corrected for the case of inelastic scattering by dividing the pixel intensity by $(\alpha + v)$, where v is the lab frame velocity and α is an adjustable parameter that

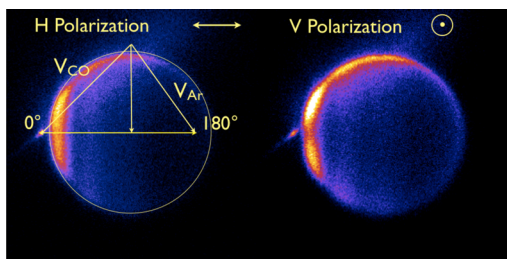


Figure 1. CO Q(9) images for CO–Ar scattering and indicated probe polarization. For the H image, the associated Newton diagram is shown. The image intensities are arbitrarily scaled relative to each other.

accounts for the finite size of the interaction volume and the finite duration of the collision event. However, as discussed in the Sensitivity section below, we determine the alignment moments with the uncorrected data. The relevant coordinate frames we employ are shown in Figure 2. Our probe laser

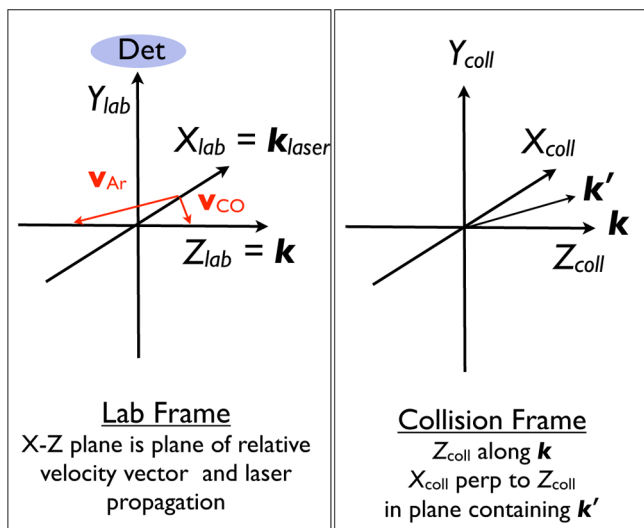


Figure 2. Coordinate frames employed. The alignment moments are defined in the collision frame.

propagation direction is in the plane of the beams, nominally perpendicular to the relative velocity vector. This defines the laboratory frame in which the Z-axis coincides with the CO beam direction in the center-of-mass, the X-axis is parallel to the laser propagation direction, and the Y-axis coincides with the time-of-flight axis. The alignment moments are obtained by analyzing the distributions in the collision frame, in which Z_{coll} again coincides with the CO beam direction in the center of mass frame, but X_{coll} is now in the plane of the scattered CO, perpendicular to Z_{coll} . Y_{coll} is then perpendicular to Z_{coll} and X_{coll} . For CO scattering in the plane of the beams, the laboratory and collision frames coincide. For scattering of CO out of the plane, the collision frame effectively represents a rotation of the laboratory frame about the Z axis. In the conventional approach, images are recorded with H or V probe laser polarizations and the difference between these is fitted by using various means to obtain the alignment moments. Our strategy instead relies on considering just three limiting distributions. We first describe intuitively how this works and how we do this analysis in practice, then we present the underlying mathematical justification.

The analysis is based upon the fact that the alignment-free differential cross section (DCS) and alignment moments may be obtained rigorously from the collision frame angular distributions for each of three orthogonal probe polarizations: one with probe laser polarization along Z_{coll} , parallel to the relative velocity vector (termed H, in-plane or “HIP”), one with the probe laser polarization parallel to Y_{coll} (this is the in-plane scattering for V polarization (V, -in-plane, “VIP”)), and finally from the scattering for probe polarization along X_{coll} . But for the in-plane scattering, X_{coll} also corresponds to the laser propagation direction, so this polarization geometry is not accessible. However, this geometry is equivalent to the collision frame that is rotated 90° from the laboratory frame for vertical polarization, as illustrated in Figure 3. If we can obtain the

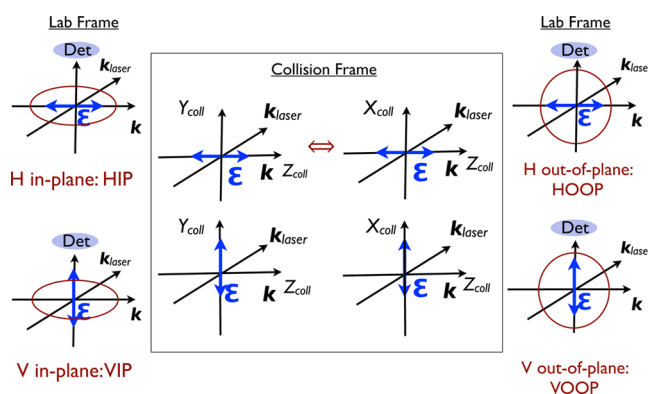


Figure 3. Relation of the lab frame and collision frame for the four angular distributions obtained from the images.

angular distribution for the products scattered perpendicular to the plane of the beams (and the detector) for V polarization, we obtain the missing geometry needed to extract the parameters directly from the distributions. We have found that by analyzing a narrow rectangular stripe along the relative velocity vector and converting this to an angular distribution, we are able to obtain the distribution corresponding to the third geometry, which we designate V, out-of-plane (“VOOP”). To obtain this distribution quantitatively, we first analyze and compare the equivalent image for H polarization (“HOOP”). In this case the two distributions HOOP and HIP should be identical. We typically adjust the limits of the region of integration (i.e., the box position and size) so that the features in the distributions are coincident. To convert from the rectangular segment to the HOOP and VOOP distributions, we first integrate pixel intensities in the segment along the width (perpendicular to the relative velocity vector), then convert the values at each point along the relative velocity vector to angle by taking the inverse cosine of the distance from the center-of-mass origin divided by the nominal recoil velocity in pixels. These are then interpolated onto the same linear grid as the in-plane distributions for further manipulation. We note that to achieve reasonable angular resolution at the poles high resolution scattering data is required. For event-counted data such as is presented here, with images at 100 pixel radius the velocity resolution at the poles for the HOOP and VOOP distributions is 8° . Lower resolution images may be employed of course, albeit with a sacrifice of detail for the first few points near the poles.

We then adjust the scaling so that the HOOP distribution has the same integral as the HIP distribution. An example of

this analysis is shown in Figure 4. When we obtain the appropriate segment of the image that gives two nearly identical

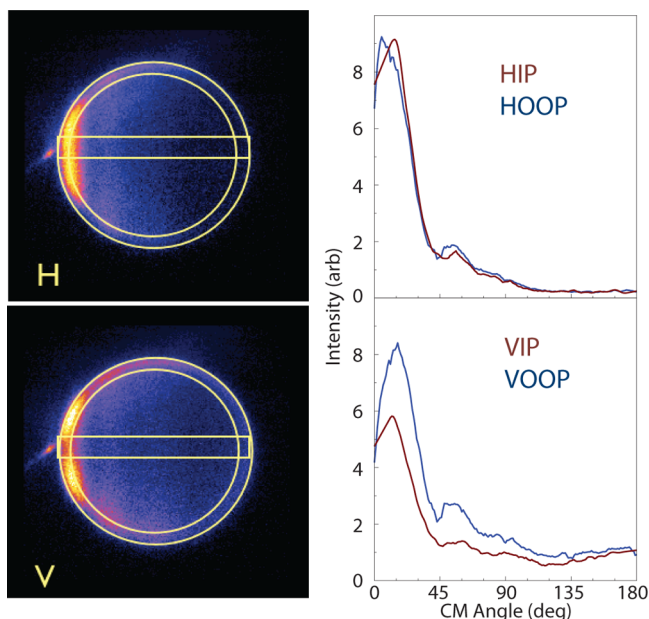


Figure 4. CO Q(9) images for indicated probe polarizations and the four distributions extracted from them. These images have been density-to-flux corrected, but as we note below, this is used in determining the full DCS but for the alignment moments we use the uncorrected images. Although the overall intensity scale for the angular distributions is arbitrary, the two plots are on the same scale.

angular distributions for H images, we employ the same rectangular image segment, integration and scaling for V images obtained under otherwise identical conditions. This yields three effective angular distributions: $I_H(\theta)$, $I_{VIP}(\theta)$, and $I_{VOOP}(\theta)$. The alignment-free differential cross sections and the polarization moments are then obtained simply as appropriate linear combinations of these three distributions. The sensitivity of the reported distributions to various aspects of the analysis is examined below. We note also that this strategy, which rests on the recognition that the angular distribution may be accurately obtained simply by integrating the region along the relative velocity vector, may find other uses, for example, in photodissociation or reactive scattering particularly involving polarization studies.

Mathematical Foundation. To obtain the form of these distributions, we loosely follow the approach of Brouard et al.,²⁵ which in turn rests on a celebrated paper of Fano and Macek,³⁴ although many have made contributions in this area. In addition to the alignment-free DCS, there are two angle-dependent parameters that embody the description of the alignment distribution for collisions of unpolarized beams: $A_0^{(2)}$ and $A_{2+}^{(2)}$. $A_0^{(2)}$ embodies the $\mathbf{v}-\mathbf{J}$ correlation, with limiting values of -1 , corresponding to $\mathbf{v} \perp \mathbf{J}$ and $+2$ corresponding to $\mathbf{v} \parallel \mathbf{J}$. $A_{2+}^{(2)}$ reflects the extent to which the \mathbf{J} vectors align parallel to

$Y_{\text{coll}}(A_{2+}^{(2)} = -1)$ or $X_{\text{coll}}(A_{2+}^{(2)} = +1)$.^{26,27} We write the signal appearing in a given angular range in the image as a product of the DCS and the detection probability:

$$I(\theta) = \frac{d\sigma}{d\theta}(\theta) P(\theta; \chi, \Theta, \phi) \quad (1)$$

The polarization-dependent transition probability $P(\theta; \chi, \Theta, \phi)$ depends on both the angular momentum polarization and the probe sensitivity to that polarization:²⁵

$$P(\theta; \chi, \Theta, \phi) = C[1 + \sum_{kq} A_q^{(k)}(\theta) F_q^{(k)}(\chi, \Theta, \phi)] \quad (2)$$

In this expression C is a constant and the $F_q^{(k)}(\chi, \Theta, \phi)$ functions are geometric factors that include the probe sensitivity as determined by the angles (χ, Θ, ϕ) characterizing the linear probe laser polarization: Θ and ϕ are the polar and azimuthal angles of $\mathbf{k}_{\text{laser}}$ in the collision frame, and χ is the third Euler angle needed to specify the laser polarization direction in that frame. These functions take the general form²⁵

$$\begin{aligned} F_0^{(2)}(\chi, \Theta, \phi) &= \frac{1}{4} h^{(2)}(j_i, j_f) (3 \sin^2 \Theta \cos 2\chi - [3 \cos^2 \Theta - 1]) \\ F_{1+}^{(2)}(\chi, \Theta, \phi) &= \frac{\sqrt{3}}{4} h^{(2)}(j_i, j_f) c_2(j_i) (2 \sin \Theta \cos \phi \sin 2\chi \\ &\quad + 2 \sin \Theta \cos \Theta \sin \phi \cos 2\chi - \sin 2\Theta \cos \phi) \\ F_{2+}^{(2)}(\chi, \Theta, \phi) &= \frac{\sqrt{3}}{4} h^{(2)}(j_i, j_f) c_2(j_i) ([1 + \cos^2 \Theta] \cos 2\phi \cos 2\chi \\ &\quad - 2 \cos \Theta \sin 2\phi \sin 2\chi - \sin^2 \Theta \cos 2\phi) \end{aligned} \quad (3)$$

They are functions of the laser polarization direction and the line strength factor $h^{(2)}$, which for Q-branch transitions is always unity.³⁴ We will confine our treatment to scattering directly in the detector plane or perpendicular to it. We then have only two polarization geometries for each of these two collision frame distributions, characterized by particular values of (χ, Θ, ϕ) and given in Table 1. Substituting these values into eq 2, we obtain the following expressions for the angular distributions in the different probe geometries:

$$I_H(\theta) = \frac{d\sigma}{d\theta}(\theta) C[1 + A_0^{(2)}(\theta)] \quad (4)$$

$$I_{VIP}(\theta) = \frac{d\sigma}{d\theta}(\theta) C \left[1 - \frac{1}{2} A_0^{(2)}(\theta) - \frac{\sqrt{3}}{2} A_{2+}^{(2)}(\theta) \right] \quad (5)$$

$$I_{VOOP}(\theta) = \frac{d\sigma}{d\theta}(\theta) C \left[1 - \frac{1}{2} A_0^{(2)}(\theta) + \frac{\sqrt{3}}{2} A_{2+}^{(2)}(\theta) \right] \quad (6)$$

We give only one H result as HIP and HOOP are identical. Table 1 and these equations show a number of key features of the polarization sensitivity. First, it is seen that the scattering signal for the H polarization has no sensitivity to the $A_{2+}^{(2)}$ parameter. This is expected given the cylindrical symmetry of this geometry. Furthermore, if we compare V and H in-plane,

Table 1. Geometric Factors for Indicated Distributions

	HIP	HOOP	VIP	VOOP
(χ, Θ, ϕ)	$(\pi, \pi/2, 0)$	$(\pi, \pi/2, \pi/2)$	$(\pi/2, \pi/2, 0)$	$(\pi/2, \pi/2, \pi/2)$
$F_0^{(2)}$	1	1	$-(1/2)$	$-(1/2)$
$F_{2+}^{(2)}$	0	0	$-(\sqrt{3}/2)$	$(\sqrt{3}/2)$

for example, by taking a difference image as is commonly done, we can eliminate the population contribution but we cannot disentangle the $A_0^{(2)}$ and $A_{2+}^{(2)}$ contributions. However, by averaging these three angular distributions together, we obtain a distribution directly proportional to the DCS, free of any polarization modulation. We can then use this to normalize the other distributions to isolate the alignment moments. By taking the difference of the VOOP and VIP distributions, we obtain a signal that is directly proportional to the $A_{2+}^{(2)}$ parameter (with the same proportionality as the DCS). Finally, the $A_0^{(2)}$ moment is obtained simply from the H distribution and the alignment-free DCS. The relevant expressions are

$$\frac{d\sigma}{d\theta}(\theta) = \frac{1}{3}[I_H(\theta) + I_{VIP}(\theta) + I_{VOOP}(\theta)] \quad (7)$$

$$A_{2+}^{(2)}(\theta) = \frac{\sqrt{3}[I_{VOOP}(\theta) - I_{VIP}(\theta)]}{I_H(\theta) + I_{VIP}(\theta) + I_{VOOP}(\theta)} \quad (8)$$

$$A_0^{(2)}(\theta) = \frac{3I_H(\theta) - [I_H(\theta) + I_{VIP}(\theta) + I_{VOOP}(\theta)]}{I_H(\theta) + I_{VIP}(\theta) + I_{VOOP}(\theta)} \quad (9)$$

The results of this analysis for the images in Figure 1 are shown in Figure 5 and compared to theory. The overall trends are reproduced quite well, but one should take note of the different scales. We have assumed the laser propagation direction is perpendicular to the relative velocity vector.

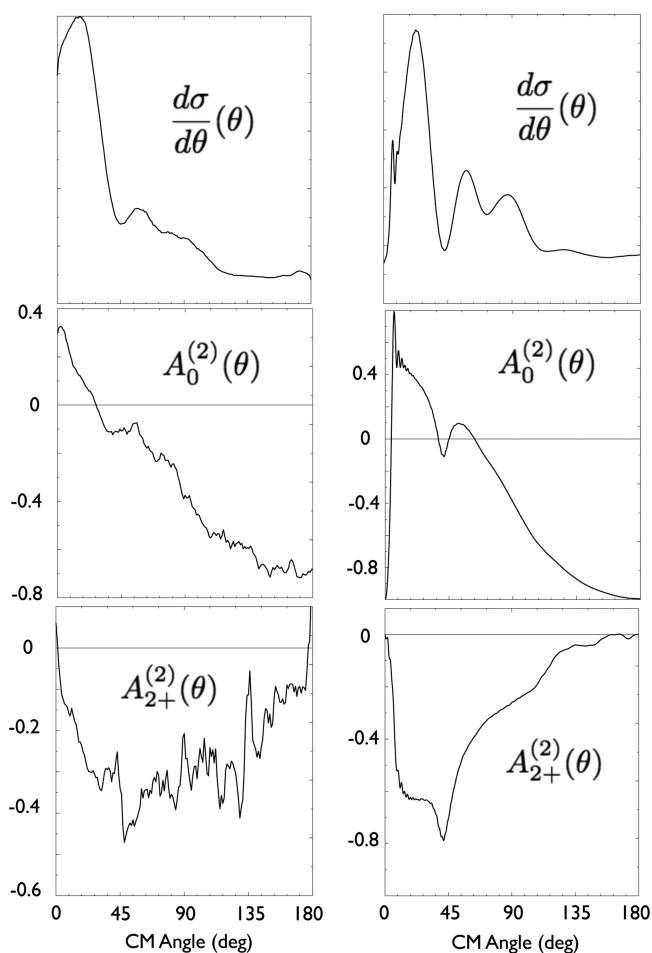


Figure 5. DCS and alignment moments obtained from the analysis (left) and from theory (right).

Deviations from this will primarily attenuate the observed alignment, and this may in part account for some of the discrepancy between the experiment and theory.

A number of qualitative features are seen in the theory and reproduced in the experimental analysis, and the details of this will be discussed in a future publication. However, we make a few observations here. The $A_0^{(2)}$ moment rises from a highly negative value in the backward direction to a positive value in the forward direction, as is widely seen and rationalized in the kinematic apse (KA) picture. In this view the collision is sudden and the angular momentum change is perpendicular to the direction of linear momentum transfer. The result is that for the directly backscattered product, the angular momentum has no projection on the recoil direction ($A_0^{(2)} = -1, \mathbf{J} \perp \mathbf{v}$), whereas in the forward direction there is a tendency to positive alignment, $\mathbf{J} \parallel \mathbf{v}$. For the pure forward scattering the projection of \mathbf{J} onto the recoil direction must vanish by symmetry, but as is usually the case, this sharp transition is not detected experimentally. The other notable feature is that the overall magnitude of the $A_0^{(2)}$ moment is consistently lower in experiment than in the theory in the backward direction. This behavior is seen in our studies involving CO scattering, and in virtually all NO studies reported previously as well. One possible explanation is the truncation of the expansion at the second moment and neglect of higher moments that might make important contributions. The $A_{2+}^{(2)}$ moment shows interesting structure in the theory that is clearly captured in the experiment. It increases from a minimum at 45° to zero for the most forward scattered product. This sharp increase in $A_{2+}^{(2)}$, and the rise in the $A_0^{(2)}$ moment in the same region, combine (owing to opposite signs) to give rise to the gap in the forward scattering for the V image (and to the forward notch in the difference images commonly shown).

Sensitivity. We also examined the sensitivity of the inferred moments and the DCS to various aspects of the analysis. One point we note is that to obtain accurate DCSs that exhibit some of the structure in the theoretical results, we must include the slow (in the lab frame) portion of the angular distribution. However, when we employ this strategy to generate the alignment moments, substantial deviations from expected values are obtained and it is difficult to obtain HIP and HOOP distributions that agree. It may be that these images are partly “sliced” so that the out-of-plane scattering is undercounted. Or there may be some nonlinearities in the detection that are equalized for the HOOP and the HIP obtained from the fast (in the lab frame) side of the scattering image. A final possibility is that stray magnetic fields or collisions perturb the alignment for the slower products. We plan future experiments to address these questions.

The general sensitivity analysis results are compiled in Figure 6. In each case we simply superimpose the results for a range of different parameter sets to convey the range of the distributions obtained. Figure 6A shows the consequence of changing the width of the rectangular “box” used for the VOOP integration from 8 to 30 pixels. It is clear that the distributions are quite insensitive to this value. Similarly, Figure 6B shows the results for changing the width of the ring integrated to give the VIP and HIP distributions over a range of 5–23 pixels. There is some slight variation in the DCS and the $q = 0$ moment, and greater associated variation in the $q = 2$ moment. Figure 6C shows the result of changing the origin of the box by up to four pixels. At this point the HIP and HOOP distributions become noticeably dissimilar, yet only the forward scattered edge of the

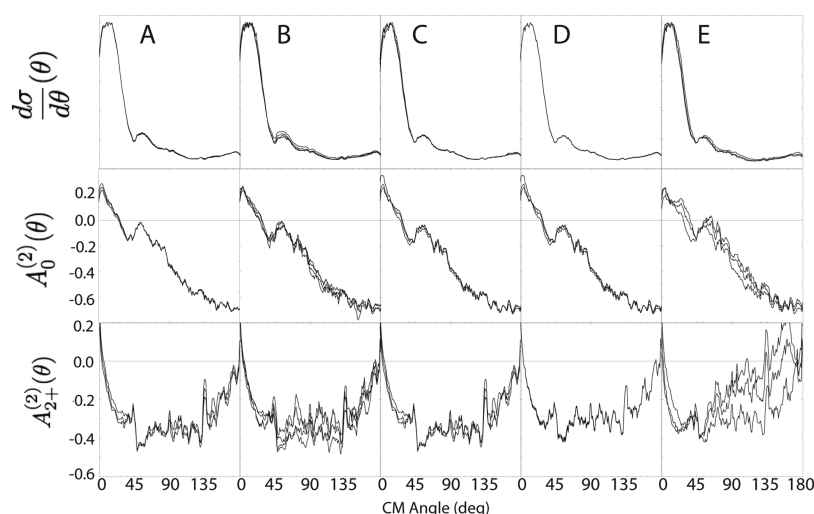


Figure 6. Results of sensitivity analysis. Variations in box width (A), ring width (B), box origin (C), relative image intensity (D), and relative image position (E) were examined (see text).

$q = 2$ moment shows any significant sensitivity to this. Figure 6D shows the result of reducing the V image intensity by 5 and 10%. There is surprisingly little variation in any of the extracted distributions in this case, which is heartening given that it is always difficult to ensure that the intensities are well controlled as the polarization is changed. The last panel, Figure 6E, shows the result of translating the V image by 2 and 3 pixels in X and Y. This has a large effect on the $A_{2+}^{(2)}$ moment and a significant effect on the $A_0^{(2)}$ moment but again little impact on the inferred DCS. This would only occur if the image focusing conditions or camera moved in the course of changing the polarization. In all, the results presented in Figure 6 show that this approach is remarkably robust. As a final comment, we note that other approaches to analysis of alignment data often incorporate full modeling of the instrument properties such as beam velocity spreads and intersection angles. We do not do this here, so this approach is restricted to well-defined experimental conditions and high-resolution images. An interesting possibility would be to combine the approach presented here with forward convolution modeling in an iterative procedure.

CONCLUSION

We have outlined a simple approach to extract alignment moments and the alignment-free DCS directly from state-resolved images of inelastic scattering. The approach is demonstrated in application to velocity-mapped images of CO scattering off argon into $J = 9$, probed via the A state. The results are compared to theoretical calculations of these moments, and good agreement is seen in many features of the distributions, although the magnitude of the alignment for the most backscattered product is underestimated, as is generally found to be the case experimentally. The approach may have other potential applications to photodissociation and reactive scattering.

AUTHOR INFORMATION

Corresponding Authors

*A. G. Suits. E-mail: asuits@wayne.edu.

*D. H. Parker. E-mail: parker@science.ru.nl.

Notes

The authors declare no competing financial interest.

ACKNOWLEDGMENTS

A.G.S. gratefully acknowledges the Radboud Excellence Initiative and support from the National Science Foundation under award number CHE-1369106. D.H.P. and G.G. acknowledge the NWO - Dutch Astrochemistry Network and DHP acknowledges the NWO - TOP project number 715.013.002 for support.

REFERENCES

- (1) Suits, A.; Bontuyan, L.; Houston, P.; Whitaker, B. Differential cross sections for state-selected products by direct imaging: Ar + NO. *J. Chem. Phys.* **1992**, *96*, 8618–8620.
- (2) Antonova, S.; Lin, A.; Tsakotellis, A. P.; McBane, G. C. State to state Ne–CO rotationally inelastic scattering. *J. Chem. Phys.* **1999**, *110*, 11742–11748.
- (3) Bontuyan, L.; Suits, A.; Houston, P.; Whitaker, B. State-resolved differential cross sections for crossed-beam argon-nitric oxide inelastic scattering by direct ion imaging. *J. Phys. Chem.* **1993**, *97*, 6342–6350.
- (4) von Zastrow, A.; Onvlee, J.; Vogels, S. N.; Groenenboom, G. C.; van der Avoird, A.; van de Meerakker, S. Y. State-resolved diffraction oscillations imaged for inelastic collisions of NO radicals with He, Ne and Ar. *Nat. Chem.* **2014**, in press.
- (5) Gilihamse, J. J.; Hoekstra, S.; van de Meerakker, S. Y.; Groenenboom, G. C.; Meijer, G. Near-threshold inelastic collisions using molecular beams with a tunable velocity. *Science* **2006**, *313*, 1617–1620.
- (6) Kay, J. J.; Steill, J. D.; Klos, J.; Paterson, G.; Costen, M. L.; Strecker, K. E.; McKendrick, K. G.; Alexander, M.; Chandler, D. W. Collisions of electronically excited molecules: differential cross-sections for rotationally inelastic scattering of NO ($A^2\Sigma^+$) with Ar and He. *Mol. Phys.* **2012**, *110*, 1693–1703.
- (7) Lorenz, K. T.; Chandler, D. W.; Barr, J. W.; Chen, W.; Barnes, G. L.; Cline, J. I. Direct measurement of the preferred sense of NO rotation after collision with argon. *Science* **2001**, *293*, 2063–2066.
- (8) Meyer, H. State-resolved cross sections and collision-induced alignment from counterpropagating beam scattering of $\text{NH}_3 + \text{He}$. *J. Phys. Chem.* **1995**, *99*, 1101–1114.
- (9) Wade, E. A.; Thomas Lorenz, K.; Chandler, D. W.; Barr, J. W.; Barnes, G. L.; Cline, J. I. Ion imaging studies of product rotational alignment in collisions of NO ($X^2\Pi^{1/2}$, $j = 0.5$) with Ar. *Chem. Phys.* **2004**, *301*, 261–272.
- (10) Brouard, M.; Chadwick, H.; Eyles, C.; Hornung, B.; Nichols, B.; Aoiz, F.; Jambrina, P.; Stolte, S.; De Miranda, M. Rotational alignment effects in NO(X) + Ar inelastic collisions: A theoretical study. *J. Chem. Phys.* **2013**, *138*, 104309.

- (11) Brouard, M.; Chadwick, H.; Eyles, C.; Aoiz, F.; Klos, J. The k_{ij} vector correlation in inelastic and reactive scattering. *J. Chem. Phys.* **2011**, *135*, 084305.
- (12) Brouard, M.; Hornung, B.; Aoiz, F. Origin of collision-induced molecular orientation. *Phys. Rev. Lett.* **2013**, *111*, 183202.
- (13) Cline, J. I.; Lorenz, K. T.; Wade, E. A.; Barr, J. W.; Chandler, D. W. Ion imaging measurement of collision-induced rotational alignment in Ar-NO scattering. *J. Chem. Phys.* **2001**, *115*, 6277–6280.
- (14) Eyles, C.; Brouard, M.; Yang, C.-H.; Klos, J.; Aoiz, F.; Gijbbers, A.; Wiskerke, A.; Stolte, S. Interference structures in the differential cross-sections for inelastic scattering of NO by Ar. *Nat. Chem.* **2011**, *3*, 597–602.
- (15) Alexander, M. H. Polarization and steric effects in inelastic collisions of NO($X^2\Pi$) with Ar and He. *Faraday Discuss.* **1999**, *113*, 437–454.
- (16) Chandler, D.; Houston, P. Two-dimensional imaging of state-selected photodissociation process detected by multiphoton ionization. *J. Chem. Phys.* **1987**, *87*, 1445.
- (17) Eppink, A. T.; Parker, D. H. Velocity map imaging of ions and electrons using electrostatic lenses: Application in photoelectron and photofragment ion imaging of molecular oxygen. *Rev. Sci. Instrum.* **1997**, *68*, 3477–3484.
- (18) Hall, G.; Sivakumar, N.; Houston, P.; Burak, I. Measurement of the angular correlation between recoil velocity and angular momentum vectors in molecular photodissociation. *Phys. Rev. Lett.* **1986**, *56*, 1671–1674.
- (19) Hall, G.; Houston, P. Vector correlations in photodissociation dynamics. *Annu. Rev. Phys. Chem.* **1989**, *40*, 375–405.
- (20) Bernstein, R.; Herschbach, D.; Levine, R. Dynamical aspects of stereochemistry. *J. Phys. Chem.* **1987**, *91*, 5365–5377.
- (21) Mestdagh, J.; Visticot, J.; Meynadier, P.; Sublemontier, O.; Suits, A. Four-vector study of the spin-changing collision Ba $[(6s)^1(6p)^1, ^1P_1(6s)^1(6p)^1, ^3P_2]/H_2$. *J. Chem. Soc., Faraday Trans.* **1993**, *89*, 1413–1418.
- (22) Balint-Kurti, G. G.; Vasyutinskii, O. S. *J. Phys. Chem. A* **2009**, *113*, 14281–14290.
- (23) Kim, Y.; Meyer, H. REMPI detection of alignment in NO collisions. *Chem. Phys.* **2004**, *301*, 273–281.
- (24) Steill, J. D.; Kay, J. J.; Paterson, G.; Sharples, T. R.; Klos, J.; Costen, M. L.; Strecker, K. E.; McKendrick, K. G.; Alexander, M.; Chandler, D. W. Rotational Alignment of NO ($A^2\Sigma^+$) from Collisions with Ne. *J. Phys. Chem. A* **2013**, *117*, 8163–8174.
- (25) Brouard, M.; Chadwick, H.; Eyles, C.; Hornung, B.; Nichols, B.; Aoiz, F.; Jambrina, P.; Stolte, S. Rotational alignment effects in NO(X) + Ar inelastic collisions: An experimental study. *J. Chem. Phys.* **2013**, *138*, 104310.
- (26) Hertel, I.; Stoll, W. Collision experiments with laser excited atoms in crossed beams. *Adv. Atom. Mol. Phys.* **1978**, *13*, 113–228.
- (27) Orr-Ewing, A.; Zare, R. Orientation and Alignment of Reaction Products. *Annu. Rev. Phys. Chem.* **1994**, *45*, 315–365.
- (28) Yan, B.; Claus, P. F. H.; van Oorschot, B. G. M.; Gerritsen, L.; Eppink, A. T. J. B.; van de Meerakker, S. Y. T.; Parker, D. H. A new high intensity and short-pulse molecular beam valve. *Rev. Sci. Instrum.* **2013**, *84*, 023102.
- (29) Tunnermann, A.; Momma, C.; Mossavi, K.; Windolph, C.; Welleghausen, B. Generation of tunable short pulse VUV radiation by four-wave mixing in xenon with femtosecond KrF-excimer laser pulses. *IEEE J. Quant. Elect.* **1993**, *29*, 1233–1238.
- (30) Hilbig, R.; Wallenstein, R. Tunable VUV radiation generated by two-photon resonant frequency mixing in xenon. *IEEE J. Quant. Elect.* **1983**, *19*, 194–201.
- (31) Wu, S.-M.; Yang, X.; Parker, D. H. Velocity map imaging study of OCS photodissociation followed by S ($1S$) autoionization at 157 nm. *Mol. Phys.* **2005**, *103*, 1797–1807.
- (32) Pedersen, T. B.; Lopez Cacheiro, J.; Fernandez, B.; Koch, H. Rovibrational structure of the ArCO complex based on a novel three-dimensional ab initio potential. *J. Chem. Phys.* **2002**, *117*, 6562–6572.
- (33) Alexander, M. H. Close-coupling studies of the orientation dependence of rotationally inelastic collisions. *J. Chem. Phys.* **1977**, *67*, 2703.
- (34) Fano, U.; Macek, J. *Rev. Mod. Phys.* **1973**, *45*, 553.